IEEE Access
Multidisciplinary | Rapid Review | Open Access Journal

Received 17 August 2022, accepted 10 September 2022, date of publication 15 September 2022,
date of current version 23 September 2022.

Digital Object Identifier 10.1109/ACCESS.2022.3206799

RESEARCH ARTICLE

Wearable Pattern-Diversity Dual-Polarized Button Antenna for Versatile On-/Off-Body Communications

TU TUAN LE, YONG-DEOK KIM, AND TAE-YEOUL YUN, (Member, IEEE)
Department of Electronic Engineering, Hanyang University, Seoul 133-791, South Korea
Corresponding author: Tae-Yeoul Yun (taeyeoul@hanyang.ac.kr)

This work was supported by the National Research Foundation of Korea under Grant 2018R1A5A7025522.

ABSTRACT A wearable dual-port button antenna that excites pattern-diversity dual-polarized waves is proposed for on-/off-body applications. Its simple structure comprises of two radiators and a common ground plane designed into two substrates. The crossed-dipole radiator is made by two symmetric bowtie dipoles printed on a circular-shaped semi-rigid substrate, which covers an ultra-wideband (UWB) application with circular polarization and directional radiation patterns, high gain, and high efficiency suitable for off-body communication. The annular-ring radiator and common ground plane are made by a conductive textile on the square-shaped flexible-felt substrate. The annular-ring radiator is shorted to the ground plane using four vias, which generates triple TMmodes covering the 2.45/5.85 GHz wireless body area networks (WBAN) with omni-directional radiation patterns and a 3.8 GHz C-band with a directional radiation pattern suitable for on-/off-body communications. The fabricated antenna is verified by measurement in both free space and phantom body environment. Measurements agreed well with simulations. Simulated specific absorption rates (SARs) under US and EU standards are below the safe level, making the proposed antenna suitable for on-/off-body communications.

INDEX TERMS Button antenna, circular polarization, dual-mode, dual-polarized, wearable antenna.

I. INTRODUCTION

Wireless body-area networks (WBANs) have drawn significant attention in the internet of things (IoTs), especially in biomedical systems for healthcare, physical training, and patient recovery progress. In such applications, the biological conditions, including body temperature, heart-rate, and blood pressure, are collected in real time by various devices. The acquired data are transferred to an external hub or station. The wearable devices allow doctors or physical trainers to monitor patients and provide spontaneous action as needed. This is known as off-body channel communication, which requires an antenna with acceptable gain and directional radiation pattern. Various types of wearable antennas are proposed for off-body communications [1], [2], [3], [4], [5], [6], [7], [8], [9], [10], [11], [12], [13]. However, all these antennas have linear polarization (LP), which may lead to polarization mismatch caused by the constant movement of the human body. To tackle this issue, circularly polarized antennas that have been used as wearable antennas can be adopted to mitigate polarization mismatch [14], [15], [16], [17], [18], [19], [20], [21]. The other communication establishes the internal links between the wearable devices on the body, called on-body channel communication, that requires an antenna with omni-directional radiation pattern to suppress the radiation in unwanted directions. Various kinds of on-body communication antennas have been presented [22], [23], [24], [25], [26], [27], [28]. Both on-body and off-body communications require the antenna with compact size, high efficiency, low specific absorption rate (SAR), and comfortability to wearers. When nodes on the body communicate each other, acquired biomedical data can be transferred to the

The associate editor coordinating the review of this manuscript and approving it for publication was Shah Nawaz Burokur.

external hub. At least, one node can establish radiation pattern diversity for both on-/off-body communications. Combining on- and off-body communication modes has recently received attention from wearable antenna designers to realize multi-mode WBAN communication. The current research efforts on multi-mode WBAN communication can be classified according to the number of frequency bands, the number of modes, or the number of excitation ports. 1) In the single-port dual-band dual-mode antenna [29], [30], [31], [32], [33], the on-body and off-body modes are operating in two different frequencies, which requires two different transceivers working with the single-port antenna and thus increases the complexity of the system. 2) The second multi-mode antenna uses the on-body and off-body modes at a single-band with a single-port [34], [35], [36], [37]. In such antennas, the radiation pattern diversity can be switched between on- and off-body mode using pin diodes. Although this kind of antenna can reduce the complexity of the system, it still has some drawbacks. First, the reconfigurability requires a large number of pin diodes, resulting in a complicated biasing circuit and a high fabrication cost. Second, the operating bandwidth is limited by a narrow band. Therefore, 3) the third type of the multi-mode antenna uses two ports with pattern diversity at the single frequency band [38], [39], [40]. One port generates an on-body mode, and the other port excites an off-body mode. This type of antenna can reduce the complexity of the system, increase the bandwidth, and reduce the fabrication cost. However, its off-body antenna communicates with LP, which can cause polarization mismatch. To tackle this issue, an interesting approach is a tri-port single-band triple-mode antenna [41]. This antenna realizes a vertical- (V-) polarized omni-directional radiation pattern for the on-body mode at one port, and horizontal- (H-) and V-polarized directional radiation patterns for the off-body mode at the two other ports. Nevertheless, the antenna structure is somewhat bulky and complicated with a triple port. In addition, the antenna operates in a single band, which limits the number of applications.

Recently, a button antenna, with its advantages, has been widely used in wearable antenna design [6], [16], [23], [29], [32], [33], [42], [43], [44]. The advantages of the button antenna over the planar antenna are as follows. 1) It can be easily mounted on clothes. 2) It allows a high-profile antenna because the main radiator and reflector of the button antenna are separately designed in two different substrates. 3) The main radiator is normally designed on a rigid substrate, which allows for the antenna with high performance. The circular polarization (CP) approach is also presented to solve polarization mismatch in button antenna design [16], [23], [32]. However, its axial ratio bandwidth (ARBW) is somewhat narrow. Furthermore, the reported button antennas are limited in either the number of application bands or polarizations. In most of the button-antenna structure, the ground plane or reflector is designed on one side of the substrate and the orther side is left unused. However, we design another radiator on the empty side, which works together with the main radiator

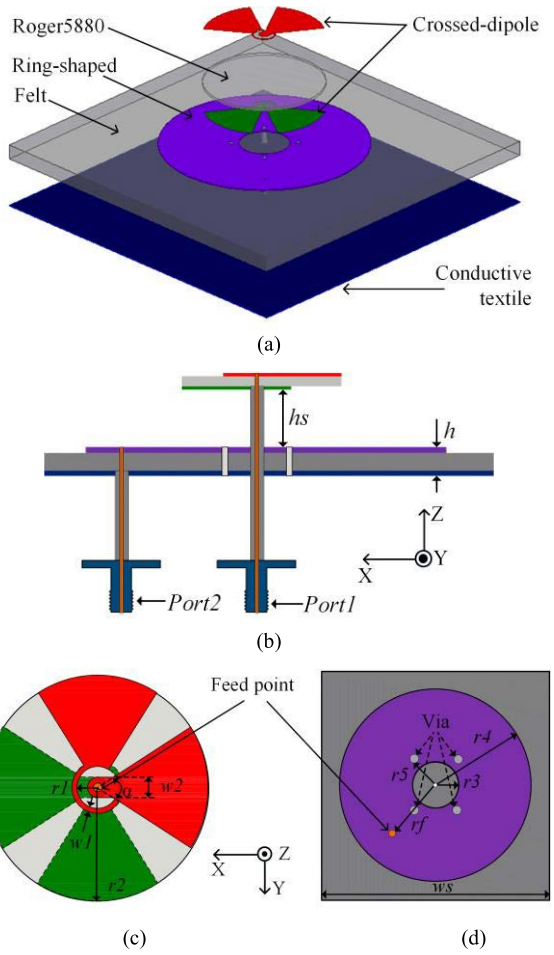

FIGURE 1. Geometry of the proposed button-antenna in: (a) perspective view, (b) side view, (c) top view of the thin semi-rigid substrate, and (d) top view of the textile substrate.

on the button substrate producing multiple-band and dual-polarization.

In this paper, we focus on the design of a simple-structure, radiation-pattern-diversity, multi-band, and dual-polarization button antenna for on-/off-body communications as presented in Section II. The button antenna consists of two radiators. The first radiator is made by a crossed-bowtie dipole printed on a rigid substrate generating an ultra-wideband, directional-radiation pattern, and a circularly-polarized wave. The crossed-dipole radiator is fed by one port. Meanwhile, an annular-ring shaped radiator and a common ground plane are printed on a felt substrate generating a triple band, on-/off-body radiation pattern, and linear polarization. The annular-ring radiator is fed by the other port. In Section III, the proposed antenna performance is tested under a deformation structure, such as bending and tilting conditions, showing its suitability for wearable applications. In Section IV, the antenna performance is measured in both free space and a phantom environment showing very good agreement between the simulations and measurements. Finally, the SARs for US and European standards are analyzed for values below

the safety regulation for wearers. Section V concludes our research.

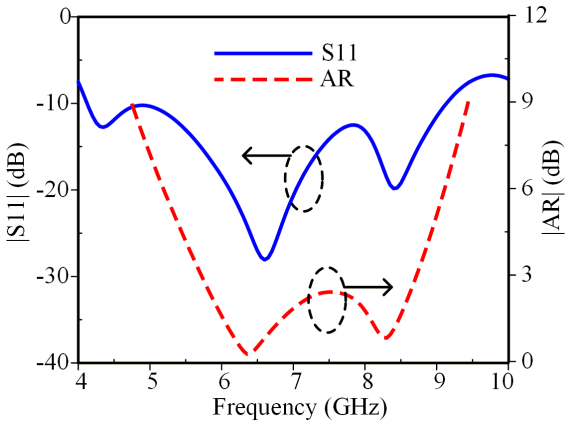

FIGURE 2. Simulated $|S_{11}|$ and AR of the crossed-bowtie dipole antenna when Port1 is excited.

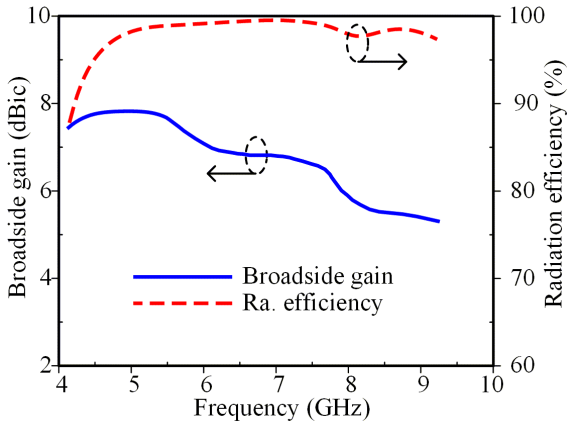

FIGURE 3. Simulated broadside gain and radiation efficiency of the crossed-bowtie dipole antenna when Port1 is excited.

In summary, the proposed wearable button antenna can address several drawbacks of previous designs: 1) use of a multi-band to adapt to various wireless applications, 2) use of a dual-mode to operate for both on-/off-body communications, 3) use of a CP bandwidth to mitigate polarization mismatch with high-gain and high-efficiency for off-body communication, and 4) a simple antenna design that is cost effective. In the authors knowledge, this is the first dual-port wearable button antenna that generates multi-band dual-mode dual-polarization for on-/off-body communications.

II. ANTENNA DESIGN AND MECHANISM

A. ANTENNA GEOMETRY

The geometry of the proposed wearable pattern-diversity multi-band dual-polarization button antenna for versatile on-/off-body communications from the perspective view, side view, and top-view is shown in Fig. 1. The proposed antenna

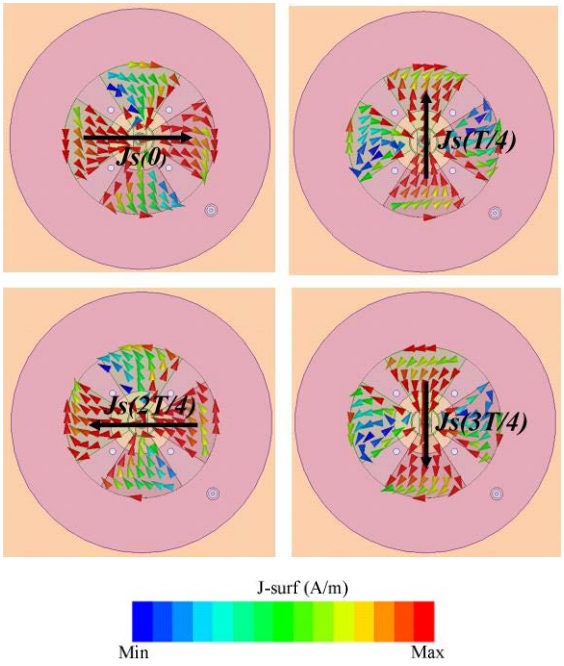

FIGURE 4. Simulated current distribution on the crossed-dipole radiator at 5.85 GHz.

is comprised of two substrates: a semi-flexible RT/Duroid 5880 substrate and a flexible felt substrate. A

crossed-bowtie dipole is designed on both sides of a circular RT/Duroid 5880 substrate with a dielectric constant of 2.2, a loss tangent of 0.001, a thickness of 0.508 mm, and a radius of 11 mm. The dipole arm is formed by a tapered-shape with a flare angle of α and a length of $r2$. Two bowtie-shaped arms are connected by a vacant-quarter ring and fed by a semi-rigid 50-Ω coaxial cable, called Port1. The vacant-quarter ring introduces a 90° phase delay between each arm of the crossed-dipole producing orthogonal E-field for every quarter period of time, thereby generating circularly polarized (CP) radiation. The crossed-bowtie dipole covers UWB applications with high-gain, high-efficiency, wide-bandwidth, circular polarization, and a directional radiation pattern, which are suitable for off-body communication. A felt substrate is placed beneath the semi-rigid substrate. The distance from the semi-flexible substrate to the felt substrate is maintained at hs. The felt substrate has a dielectric constant of 1.4, a loss tangent of 0.044, a width of ws, and a thickness of h. The annular ring-shaped radiator and a square-shaped ground plane are made of a ShielditTM super conductive textile with a conductivity of 118,000 S/m, which are adhered to the frontside and backside of the felt substrate, respectively. The square-shaped ground plane acts as a common ground plane for the crossed-bowtie dipole and annular-ring radiators. The annular-ring radiator has an inner and outer radius of $r3$ and $r4$, respectively. The annular- ring radiator is shorted to the ground plane using four shorting-vias with the distance to the center of $r5$, as shown in Fig. 1 (d). The annular-ring radiator is fed

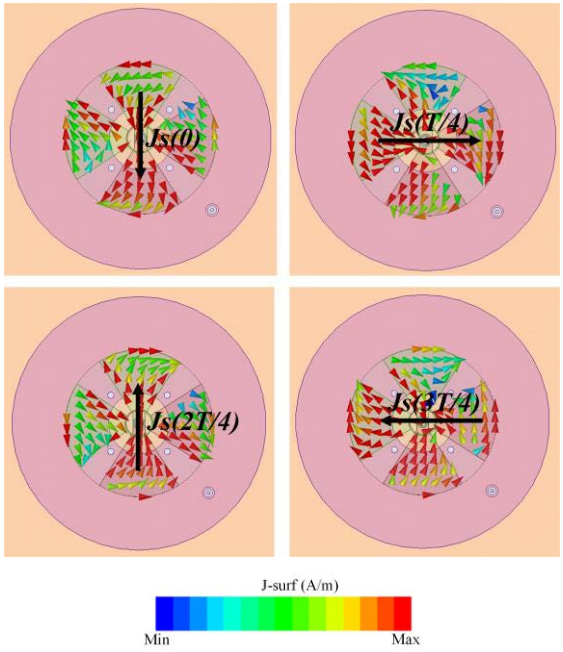

FIGURE 5. Simulated current distribution on the crossed-dipole radiator at 7.6 GHz.

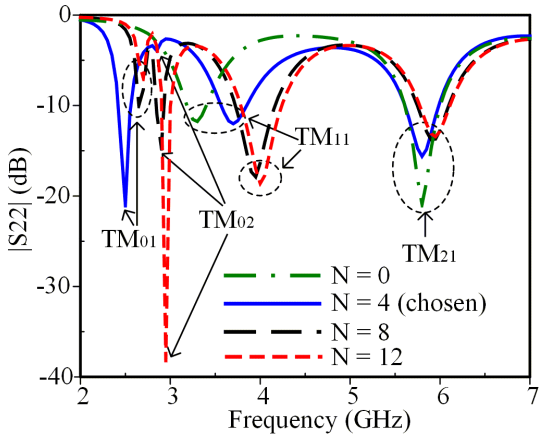

FIGURE 6. Simulated $|S_{22}|$ annular-ring antenna with a various number of shorting-vias when exciting Port2.

by another coaxial cable located at distance rf, called Port2, as shown in Fig. 1 (b) and Fig. 1 (d). The annular-ring radiator yields linearly polarized waves with an omni-directional radiation pattern at two bands and a directional radiation pattern at the other band. Therefore, it has radiation pattern diversity for both on-body and off-body communications. The SAR is significantly minimized while the user's comfort is maintained because of the common flexible ground plane.

The button antenna was characterized using the ANSYS high-frequency structure simulator. The optimized geometrical parameters are: $r1 = 2.1$, $w1 = 0.2$, $w2 = 2$, $r2 = 11$, $r3 = 5$, $r4 = 20.7$, $r5 = 5$, $rf = 6.5$, $ws = 50$, $hs = 12$, $h = 3$, and $\alpha = 65$ degrees (unit: mm).

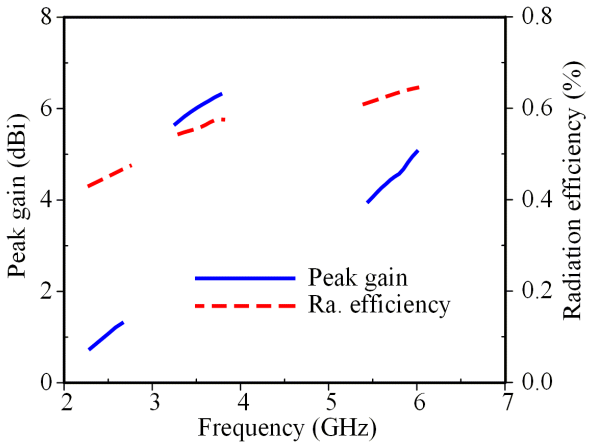

FIGURE 7. Simulated peak-gain and radiation efficiency of the annular-ring antenna when Port2 is excited.

B. SIMULATED RESULTS AND WORKING MECHANISM

1) CROSSED-DIPOLE RADIATOR

Figure 2 plots the simulated $|S_{11}|$ and axial ratio (AR) characteristics of the crossed-bowtie dipole radiator when Port1 is excited. The dipole arm, r_2, is approximately $\lambda_0/4$ at center frequency of 6.8 GHz. The radiator yields an impedance bandwidth (IBW) of 75.5% (4.12–9.12 GHz), nearly covering the entire UWB application. The crossed-bowtie dipole radiator exhibits a very wide 3-dB axial-ratio bandwidth (ARBW) of 41.39% (5.71–8.69 GHz). The peak gain and radiation efficiency within the IBW are plotted in Fig. 3. The maximum peak gain of 8 dBic is achieved at approximately 8 GHz, and the radiation efficiency is greater than 92% over the entire IBW.

In order to explain the circular polarization mechanism of the crossed-bowtie dipole radiator, the simulated current distributions on the crossed-bowtie dipole radiator at 5.85 and 7.6 GHz within a time period of $t = 0, t = T/4, t = 2T/4$, and $t = 3T/4$ are shown in Figs. 4 and 5, respectively, where T is the period of time and J_s is the vector summation of the major current distribution. The CP radiation at 5.85 and 7.6 GHz are generated by induced currents on the crossed-dipole arm. At t = 0, dominant currents flow in horizontal and vertical arms at 5.85 and 7.6 GHz, respectively. As we increase the period of time by T/4, J_s at different time instances is rotated 90° in counter-clockwise direction and equal in magnitude, thereby generating right-hand circular polarization (RHCP) in the $+z$ direction.

2) ANNULAR-RING RADIATOR

The annular-ring resonator is fed by Port2. To understand the working mechanism, simulated $|S_{22}|$ with a different number of shorting-vias (N = 0, 4, 8, 12) is investigated, as shown in Fig. 6.

For N = 0, the resonant frequency for the lowest mode TM_{01} mode is zero. Only the TM_{02}, TM_{11}, and TM_{21} modes at high frequency are excited. The mode identification based

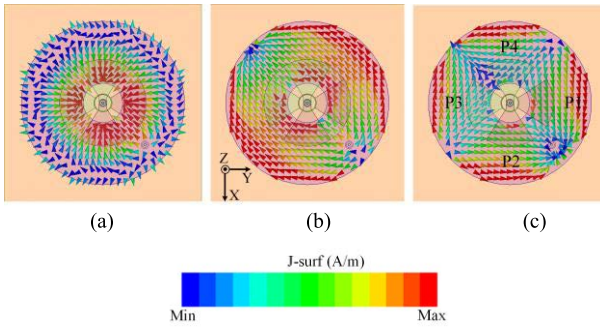

FIGURE 8. Normalized surface current distributions on the annular-ring antenna at (a) 2.45 GHz, (b) 3.6 GHz, and (c) 5.85 GHz.

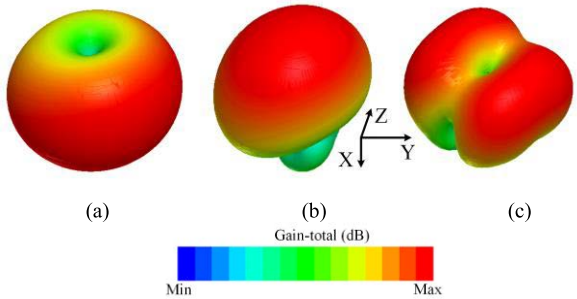

FIGURE 9. Normalized 3-D radiation pattern of the annular-ring antenna at (a) 2.45 GHz, 3.6 GHz, and (c) 5.85 GHz.

on fringing fields at the inner and outer peripheries is presented in [45]. The resonant frequencies of TM_{11} and TM_{21} are 3.3 and 5.8 GHz, respectively. The TM_{02} mode is not observed because of its poor impedance matching.

For N > 0, when the annular-ring is loaded with shorting-vias, an additional mode of TM_{01} at a lower frequency range is excited. By increasing the number of shorting-vias to N= 4, the TM_{01} mode is excited at a resonant frequency of 2.45 GHz, and the TM_{02} mode appears at a frequency of approximately 3.0 GHz. Poor impedance matching is still observed at the TM_{02} mode. By increasing the number of shorting-vias (N = 8, 12), the resonant frequency of TM_{01} increases while the resonant frequency of the TM_{02} mode slightly increases. Increasing N decreases the area of the annular-ring. Therefore, it decreases the capacitance of the annular-ring, which increases the resonant frequencies of TM_{01} and TM_{02}. By optimization of the number of shorting-vias and via radius, r_5, the annular-ring antenna excites the TM_{01}, TM_{11}, and TM_{21} modes at approximately 2.45, 3.8, and 5.85 GHz, respectively. The simulated IBWs are 6.45% (2.40–2.56 GHz), 9.35% (3.57–3.92 GHz), and 6.6% (5.61–6.0 GHz), which cover 2.45/5.85 GHz WBAN and 3.8 GHz C-band applications. The overlap operating frequency between the annular-ring and the crossed-bowtie dipole radiators is 6.6% (5.61–6.0 GHz), which enables on-body/off-body WBAN communication at 5.8 GHz.

The simulated peak-gain and radiation efficiency within the operating bandwidth are shown in Fig. 7. The peak-gains

TABLE 1. Proposed antenna performance summary.

Port	f_0 (GHz)	Polarization state (LP/CP)	On-/Off-body
Port1	UWB	CP	Off-body
Port2	2.45	LP	On-body
	3.7	LP	Off-body
	5.85	LP	On-body

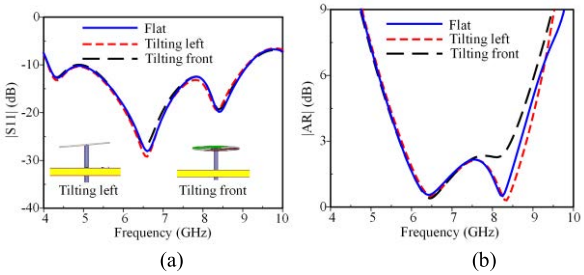

FIGURE 10. Simulated (a) $|S_{11}|$ and (b) AR of the crossed-bowtie dipole radiator in flat and tilting conditions.

range from 1 to 6.6 dBi, while low radiation efficiencies from 47% to 63% are achieved because of the lossy felt substrate. The low peak-gain at 2.45 GHz is additionally caused by its omni-directional radiation pattern, which is described below in detail.

To investigate the operating mechanism of each mode, the simulated surface current distributions and 3-D radiation patterns of the TM_{01}, TM_{11}, and TM_{21} modes are shown in Figs. 8 and 9, respectively. The current distributions of the via-loaded TM_{01} mode at 2.45 GHz are concentrated inside the cavity, *r5*, near the inner rim as shown in Fig. 8 (a), and yield an omni-directional radiation pattern as shown in Fig. 9 (a). The strong current distributions of TM_{11} at 3.6 GHz occur at both the inner rim, *r3*, and outer rims, *r4*, of the annular-ring, as shown in Fig. 8 (b), which radiates the directional radiation pattern in Fig. 9 (b). In Fig. 8 (c), the TM_{21} current distribution at 5.85 GHz is strong at the outer rim, *r4*, of the annular-ring radiator. The current is distributed in four parts (P1, P2, P3, and P4), which are symmetric over the diagonal. As a result, the 3-D radiation pattern is divided into two main beams and null in the broadside direction, as shown in Fig. 9 (c).

The proposed button antenna performances, including the resonant frequency, polarization state, and on-/off-body communication type are summarized in Table 1. Port1 excites the ultra-wideband CP mode with off-body communication. Port2 excites three LP modes with on-/off-body communications.

3) DESIGN PROCEDURE

Based on the abovementioned analysis, the design procedure can be divided into three main sections: design of the annular-ring radiator (*Step1* and *Step2*), crossed-dipole radiator (*Step3*), and fine tuning of the entire structure (*Step4* and *Step5*).

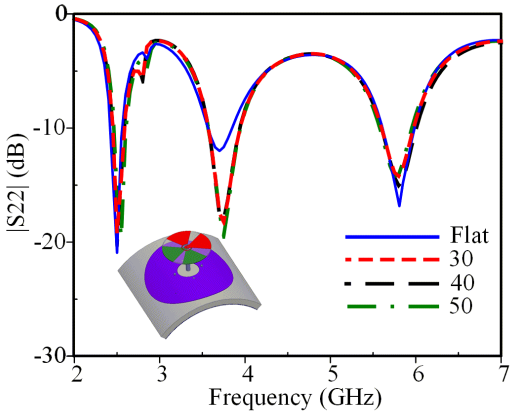

FIGURE 11. Bending effect of the annular-ring radiator in the *x*-direction.

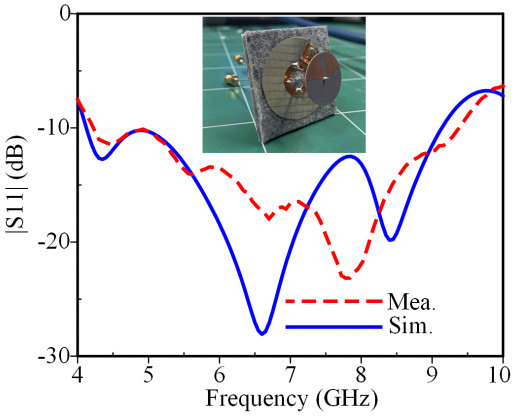

FIGURE 12. Simulated and measured $|S_{11}|$ of the crossed-bowtie dipole radiator in free space.

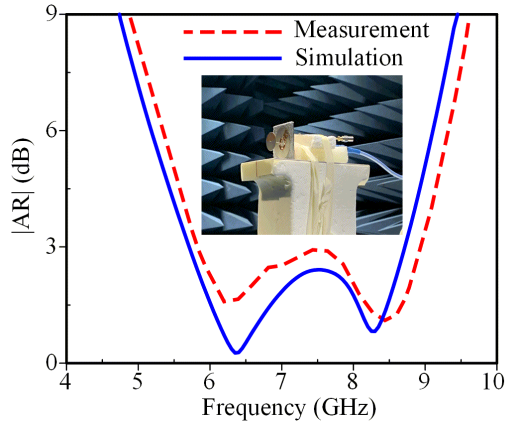

FIGURE 13. Simulated and measured AR of the crossed-bowtie dipole radiator in free space.

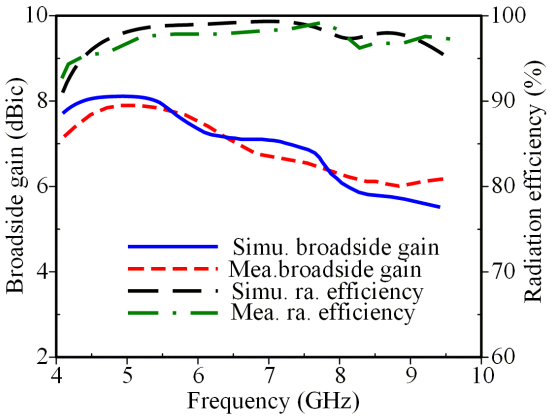

FIGURE 14. Simulated and measured broadside gain and radiation efficiency of the crossed-bowtie dipole radiator in free space.

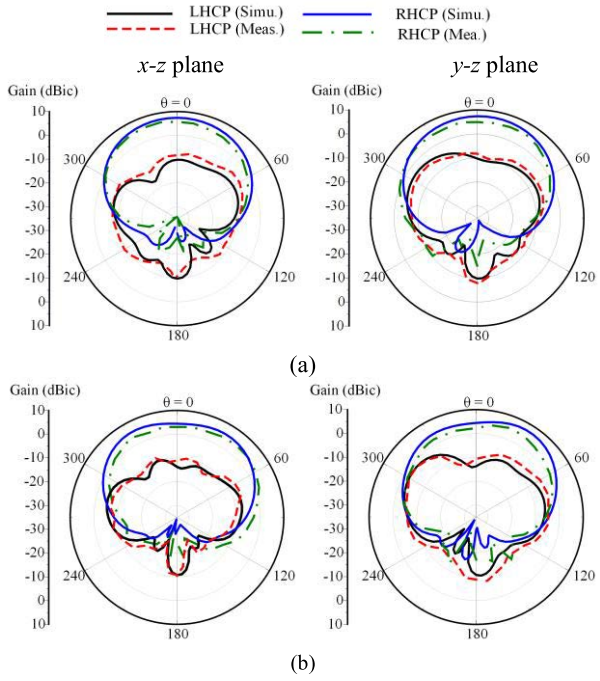

FIGURE 15. Simulated and measured radiation patterns of the crossed-bowtie dipole radiator in free space at (a) 5.85 GHz and (b) 7.6 GHz.

Step 1: Design the annular-ring radiator without the shorting-vias and choose the initial value for outer radius, *r4*, to achieve a TM_{21} mode at approximately 5.8 GHz.

Step 2: Add the shorting-vias to the annular-ring and optimize the number of shorting-vias, N, and via radius, *r5*, to achieve a TM_{01} at approximately 2.5 GHz. Optimize the outer radius, *r4*, again to achieve TM_{11} at approximately 3.5 GHz.

Step 3: Design the crossed-dipole radiator with the dipole arm, *r2*, with a quarter-wavelength ($\lambda_0/4$), where λ_0 is the wavelength referring to the frequency of 6.8 GHz, the center frequency of UWB applications. Optimize the flare-angle α and width of the quarter-ring, *w1*, to achieve optimum IBW.

Step 4: Optimize the quarter-ring radius, *r1*, providing a phase difference of 90° among the crossed-bowtie dipole arms to achieve the maximum ARBW. Optimize the height of the crossed-bowtie dipole antenna, *hs*, to achieve the maximum broadside gain and reduce the radiation pattern

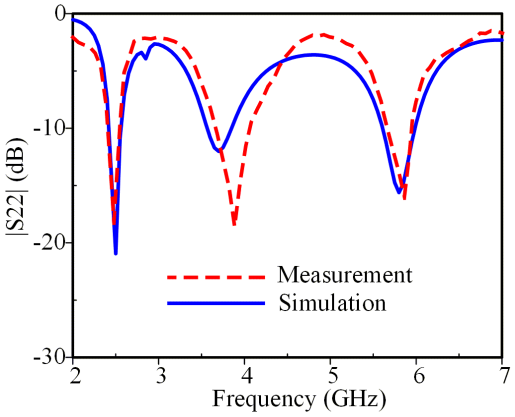

FIGURE 16. Simulated and measured S_{22} of the annular-ring radiator in free space.

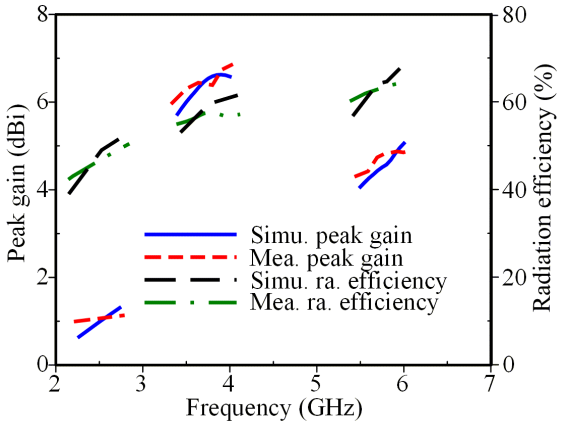

FIGURE 17. Simulated and measured peak gain and radiation efficiency of the annular-ring radiator in free space.

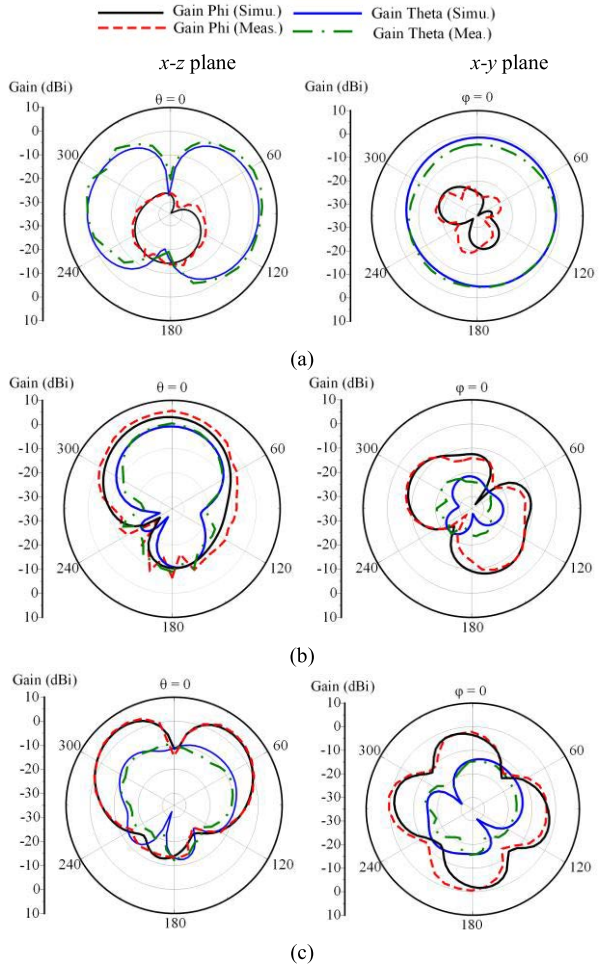

FIGURE 18. Simulated and measured radiation patterns of the annular-ring radiator in free space at (a) 2.45 GHz, (b) 3.8 GHz, and (c) 5.85 GHz.

distortion of the annular-ring radiator caused by the semi-rigid substrate.

Step 5: Final tune all parameters for an optimized design.

III. DEFORMATION STUDIES

We investigate the antenna performance in a deformation situation, such as bending and tilting effects on the annular-ring and crossed-bowtie dipole radiators. Because of the symmetric geometry, only bending in the x-direction is considered for the annular-ring radiator. Additionally, only tilting in the front and tilting in the left are considered for the crossed-bowtie dipole radiator.

To investigate the tilting effect, the crossed-bowtie dipole radiator is tilted at an angle of 5°, as shown in Fig. 10. As a result, there is no effect on the $|S_{11}|$ parameter, as shown in Fig. 10 (a). However, there is a slight effect on the ARBW, as shown in Fig. 10 (b). The AR mode at high frequencies seems to be slightly diminished when the antenna is tilted in the front. Simulated $|S_{22}|$ results of the annular-ring radiator bending along the cylinder with radii of 30, 40, and 50 mm compared with the flat condition are shown in Fig. 11. The bending effect is slightly observed on the $|S_{22}|$ parameter; however, the resonant frequencies remain unchanged.

The deformation investigation demonstrates that the proposed antenna can work well without severe changes in bending or tilting conditions.

IV. MEASUREMENT RESULTS

To validate the simulated results and confirm the suitability for on-/off-body communications, the proposed antenna is fabricated and measured in an anechoic chamber. The fabricated button antenna is shown in the inset in Fig. 12.

A. FREE SPACE PERFORMANCE

1) CROSSED-DIPOLE RADIATOR

The S-parameters and far-field performances of the crossed-bowtie dipole radiator are measured at Port1. During the measurement, when one port is being measured, the other port is terminated to a load of 50 Ω. The measured $|S_{11}|$ in Fig. 12 shows a wide IBW of 75.3% (4.14–9.14 GHz), which nearly covers the entire UWB application band. The measured result of the ARBW in Fig. 13 shows 41.71% (5.75–8.78 GHz). The measured broadside gain and radiation

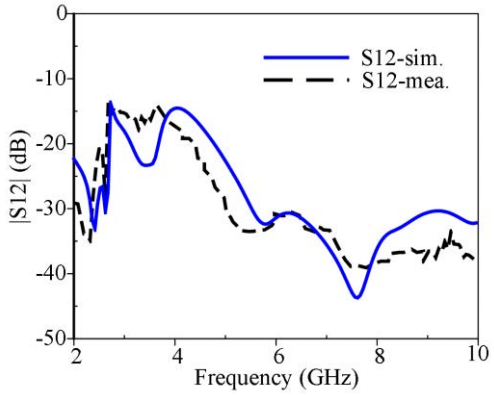

FIGURE 19. Simulated and measured $|S_{12}|$ in free space.

TABLE 2. Human tissue.

Layer	Permittivity	Conductivity	Mass Density
Skin	35.11	3.72	1100
Fat	4.95	0.29	910
Muscle	48.48	4.96	1041

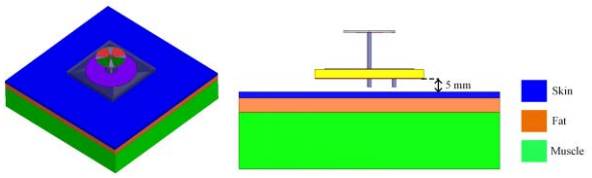

FIGURE 20. Three-layered human tissue.

efficiency are shown in Fig. 14. The measured broadside gain is greater than 6 dBic with a peak of 8 dBic at approximately 5.5 GHz. The measured radiation efficiency is greater than 90%. The measured radiation patterns of the crossed-bowtie dipole radiator in two principle planes x-z and y-z at 5.85 and 7.6 GHz are plotted in Fig. 15. The crossed-bowtie dipole radiator radiates directional radiation pattern characteristics with right-hand circular polarization in the $+z$ direction, which is suitable for off-body communication applications. Furthermore, the measured front-to-back ratios (FBRs) at 5.85 and 7.6 GHz in the $+z$ direction are greater than 15 dB, which indicates that little energy is radiated into the backward radiation. The simulated and measured results are in good agreement.

2) ANNULAR-RING RADIATOR

The performance of the annular-ring radiator is measured at Port2. The measured IBW of $|S_{22}|$ is shown in Fig. 16. The measured IBW is achieved of 5.62% (2.42–2.56 GHz), 13% (3.6–4.1 GHz), and 5.86% (5.63–5.97 GHz), which covers the 2.45/5.85 GHz WBAN band and 3.8 GHz C-band applications. The measured broadside-gain and radiation efficiency within the operating bandwidth are shown in Fig. 17. The measured maximum peak-gains within three bands are achieved of 1.05, 6.6, and 4.9 dB, respectively. The measured

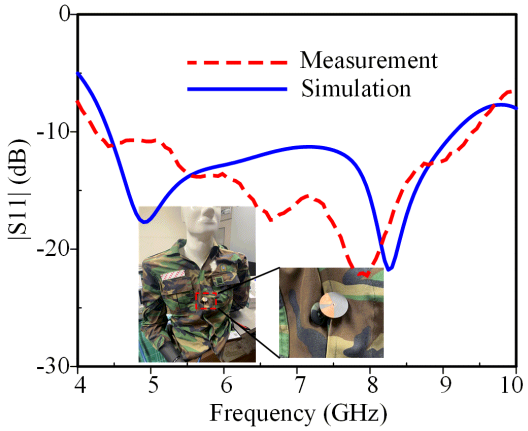

FIGURE 21. Simulated and measured $|S_{11}|$ of the crossed-bowtie dipole radiator on the human phantom.

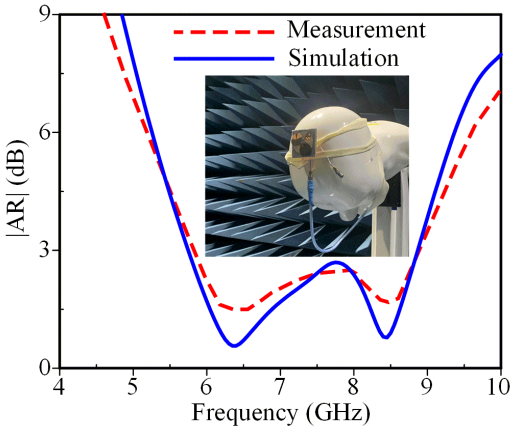

FIGURE 22. Simulated and measured AR of the crossed-bowtie dipole radiator on the human phantom.

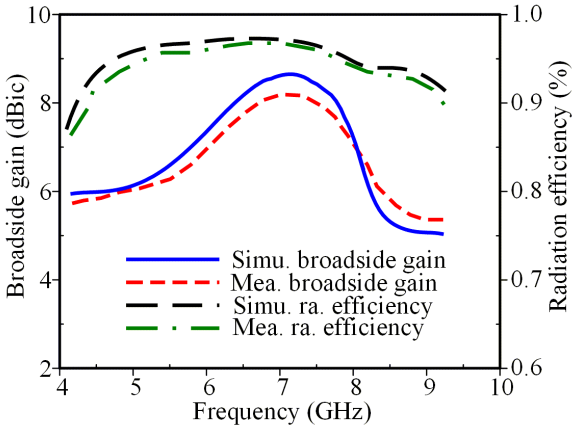

FIGURE 23. Simulated and measured broadside gain and radiation efficiency of the crossed-bowtie dipole radiator on the human phantom.

radiation efficiencies are 44%, 56%, and 64%, which are relatively low because of the lossy felt substrate used for the annular ring radiator. The measured radiation patterns in the two principle x-z and x-y planes of the annular-ring

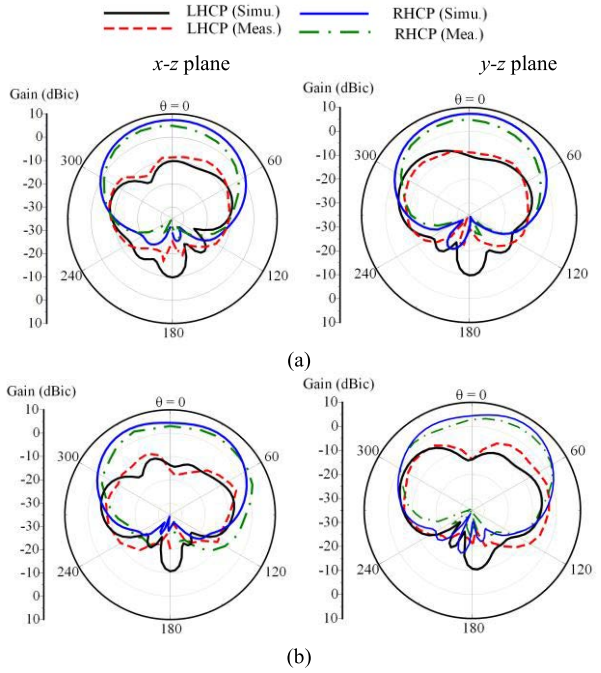

FIGURE 24. Simulated and measured radiation patterns of the crossed-bowtie dipole radiator on the human phantom at (a) 5.85 GHz and (b) 7.6 GHz.

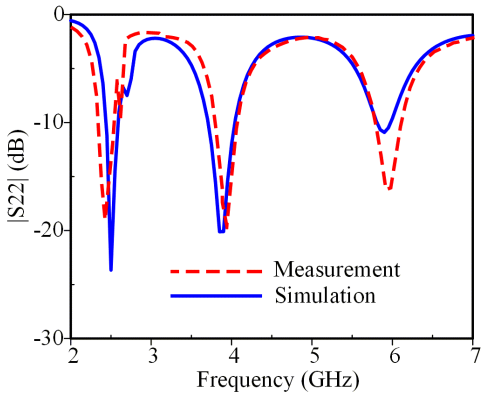

FIGURE 25. Simulated and measured $|S_{22}|$ of the annular-ring radiator on the human phantom.

radiator at 2.45, 3.8, and 5.85 GHz are shown in Fig. 18. The directional radiation pattern is observed at 3.8 GHz with a high FBR of 14 dB. Low cross polarization discrimination is observed in the $+z$ direction because of the symmetrical current distribution on the annular-ring radiator around the diagonal, as shown in Fig. 8 (b). Monopole-like radiation patterns are observed at 2.45 and 5.85 GHz with the main beam at 90° and 45°, respectively. An omnidirectional pattern is observed at 2.45 GHz in Fig. 18 (a). A null-beam for each quarter angle is observed in the horizontal plane at 5.85 GHz in Fig. 18 (c). The current distribution is divided into four parts, which is symmetry over the diagonal as shown in Fig. 8 (c). The mutual coupling between two ports, $|S_{12}|$, in the frequency range of 2-10 GHz is shown in Fig. 19. As a result, the mutual coupling

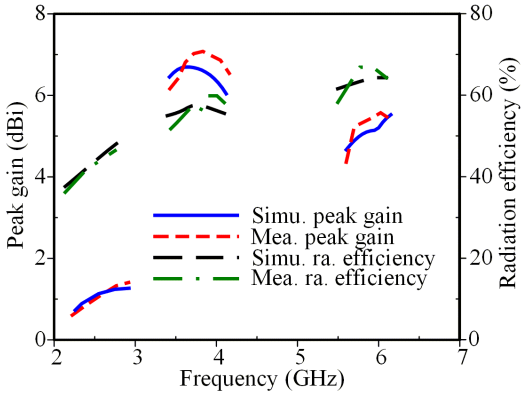

FIGURE 26. Simulated and measured peak gain and radiation efficiency of the annular-ring radiator on the human phantom.

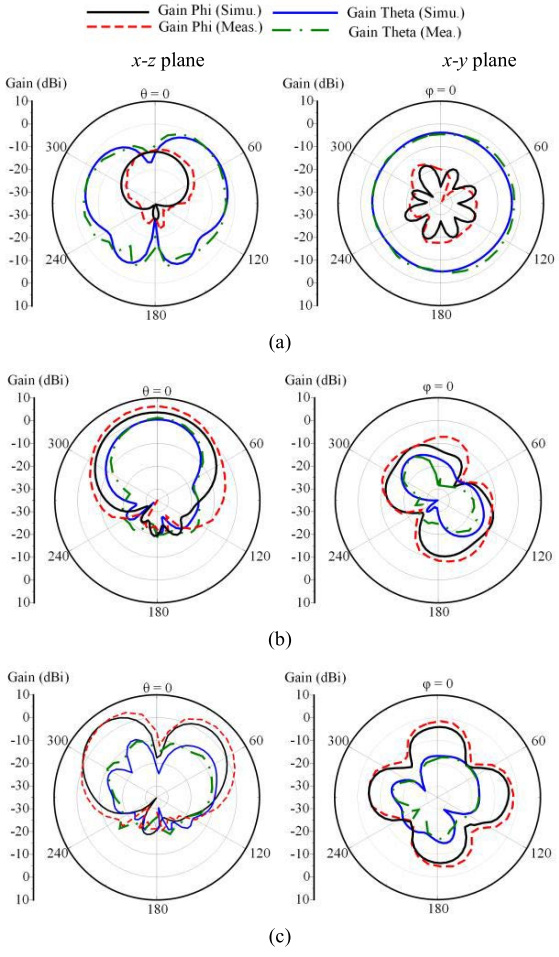

FIGURE 27. Simulated and measured radiation patterns of the annular-ring radiator on the human phantom at (a) 2.45, (b) 3.8, and (c) 5.85 GHz.

of $|S_{12}|$ is below -20 dB from 4 to 10 GHz. High mutual coupling is observed from 3 to 4 GHz. This is because the annular-ring radiator has directional radiation pattern at this frequency range, as shown in Figs. 9 and 18. The mutual coupling can be reduced by increasing crossed-dipole radiator's height, *hs*.

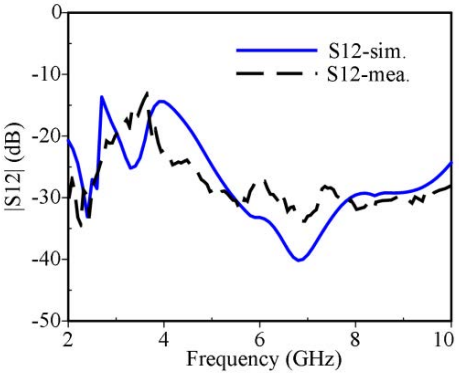

FIGURE 28. Simulated and measured $|S_{12}|$ in the phantom body.

B. ON-BODY PERFORMANCE

In this section, the antenna performances in the presence of a phantom-body and human body-like environment are performed. The antenna is placed 5 mm from the $160 \times 160 \times 27$ mm^3 three-layered human body-like environment, as shown in Fig. 20. The thickness of the skin, fat, and muscle are 2, 5, and 20 mm, respectively. The relative permittivity, conductivity, and mass density [1] at 5.85 GHz are listed in Table 2. The *S*-parameters and radiation pattern measurements are performed in the phantom body environment.

1) CROSSED-DIPOLE RADIATOR

The proposed button antenna is mounted on the phantom body. Where the crossed-bowtie dipole radiator is exposed in the front of the cloth, the annular-ring radiator is hidden below the cloth, as shown in the inset in Fig. 21. As a result, the measured $|S_{11}|$ in the phantom environment is 72.8% (4.32–9.22 GHz) compared to simulated result of 69.4% (4.43-9.14 GHz). The small difference between the simulated and measured $|S_{11}|$ might be caused by the effect of cloth on the phantom body during the measurement. The fabricated antenna is mounted on the phantom head for measurement in an anechoic chamber showing a wide ARBW of 42.7% (5.75–8.87 GHz), as shown in Fig. 22. The measured broadside gain and radiation efficiency are shown in Fig. 23. The measured broadside gain is greater than 5 dBic with a peak of 8.4 dBic at a frequency of approximately 8 GHz. The measured radiation efficiency within the IBW is greater than 86%, as shown in Fig. 22. The RHCP radiation pattern in the two principle *x*-*z* and *y*-*z* planes at 5.85 and 7.6 GHz are shown in Fig. 24. The measured FBRs at 5.85 and 7.6 GHz are greater than 27 dB, which is greater than the results measured in free space.

2) ANNULAR-RING RADIATOR

Fig. 25 shows the measured results of $|S_{22}|$ on the phantom body environment. The simulated and measured results are in good agreement. The measured $|S_{22}|$ exhibits IBWs of 5.56% (2.41–2.55 GHz), 8.25% (3.72–4.04 GHz), and 5.37% (5.8–6.12 GHz). The measured peak gain and radiation efficiency are shown in Fig. 26. The measured peak-gains achieved at 2.45, 3.8, and 5.85 GHz are 1, 6.6, and 5.05 dBi, respectively. The measured radiation-efficiencies achieved at 2.45, 3.8, and 5.85 GHz are 42%, 51%, and 61%, respectively. The measured radiation patterns in the two principle *x*-*z* and *x*-*y* planes at 2.45, 3.8, and 5.85 GHz are shown in Fig. 27. Radiation pattern shapes similar to those observed in free space were observed. As a result, the radiation pattern is observed at 3.8 GHz with a measured FBR of 22.5 dB. The monopole-like radiation pattern is observed at 2.45 and 5.85 GHz with the main beam at 90° and 45°, respectively. An omnidirectional radiation pattern is observed at 2.45 GHz and a radiation pattern with four nulls is observed at 5.85 GHz in the *x*-*y* horizontal plane. The measured mutual coupling between two ports, $|S_{12}|$, in the phantom body environment is shown in Fig. 28. It can be seen that the measured $|S_{12}|$ are below -20 dB within the operating bandwidth of the crossed-dipole and annular-ring radiator.

In summary, antenna performance measurements are performed both in free space and in a phantom body environment. The results in the phantom body show slight degradation in terms of impedance bandwidth, peak gain, and radiation efficiency compared with the results in free space. This decrease is caused by the proximity effect and ground plane bent over the phantom body during the measurement. The measured FBR in the phantom body is greater than in free space because the phantom body works as a reflector reflecting electromagnetic waves in backward radiation.

TABLE 3. Summary of simulated SAR.

Port	Frequency (GHz)	Mass tissue (g)	SAR (W/kg)
Port1	5.85	1	0.19
	7.6	1	0.15
	5.85	10	0.06
	7.6	10	0.05
Port2	2.45	1	1.5
	3.8	1	0.83
	5.85	1	0.36
	2.45	10	0.74
	3.8	10	0.32
	5.85	10	0.13

C. SAR ANALYSIS

The SAR values are simulated for both the crossed-dipole and the annular-ring radiator based on US and European standards with the excitation of Port1 and Port2, respectively. The US standard sets a limit of 1.6 W/kg for 1 g average mass and the European standard sets a limit of 2 W/kg for 10 g average mass. The chosen input power is 500 mW.

The simulated SARs when exciting Port1 for the US standard at frequencies of 5.85 and 7.6 GHz are 0.19 and 0.15 W/kg, respectively. Meanwhile, simulating SARs with the European standard are 0.06 and 0.05 W/kg, which is significantly less than its standard values. When exciting Port2, the simulated SARs for the US standard at 2.45, 3.8, and 5.85 GHz are 1.5, 0.83, and 0.36 W/kg, respectively. With the European standard, the simulated SAR values are 0.74, 0.32, and 0.13 W/kg.

TABLE 4. Comparison with other antennas in the literature.

Ref.	f_0 (GHz)	BW (%)	Efficiency (%)	Gain (dBi)	Antenna Size (λ_0^3)	SAR (W/kg)	Number of Port	LP/CP
[1]	2.45/3.0/3.45	4.4/4.0/6.2	79/83/82	4.2/6.6/5.0	0.5 × 0.5 × 0.06	0.13/0.09/0.09	1	LP
[4]	3.5/5.8	29/8.74	83/91	9.3/6.6	1 x 1 x 0.05	0.34/1.65	1	LP
[15]	5.8	6.9	>70	6.0	0.76 x 0.88 x 0.05	0.95	1	CP
[23]	5.8	3.97	72.6	2.1	0.3 × 0.3 × 0.2	0.12*	1	CP
[28]	4.8	34	N/A	6.1	1.7 × 1.13 × 0.06	1.18	1	LP
[30]	2.45/5.8	4.8/3.7	53.6/70.1	5.8/6.9	0.82 × 0.82 × 0.016	0.042/0.09	1	LP/CP
[32]	2.45/6.5	7/52	N/A	2.2/8.6	0.51 × 0.51 × 0.08	1.04/ 0.29*	1	LP/CP
[33]	2.45/5.8	N/A	46.3/69.3	-0.6/4.3	0.2 × 0.2 × 0.02	2.52*	1	LP
[38]	2.45	N/A	92/93	N/A	0.56 × 0.56 × 0.05	N/A	2	LP
[41]	5.05	14	>93	5.8/11.2/10.8	1 × 1 × 0.09	1.99	3	LP
[23]	5.8	3.97	72.6	2.1	0.55 × 0.55 × 0.2	0.118	1	CP
[44]	4.55/5.3	2.4/8.7	86/93	7.5/7.6	0.29 × 0.29 × 0.28	0.06/0.09	2	HP/VP
Prop.	2.45/3.7/5.8/UWB	5.5/8.2/5.3/72.8	42/51/61/86	1/6.6/5.05/6.5	0.4 × 0.4 × 0.12	1.5/0.83/0.36/0.06	2	LP/CP

λ_0 is the wavelength at lowest resonant mode.
* indicates simulated SAR under US standard for 1 g average mass.

The summary of simulated SAR for Port1 and Port2 is listed in Table 3. The simulated SAR value at 2.45 GHz is greater than other frequencies, primarily because of its omni-directional radiation pattern with the main beam around 90° as shown in Fig. 9. The SAR of Port1 is significantly smaller than Port2 because the annular-ring radiator is placed close to human body. In addition, it has omni-directional radiation patterns, which radiates toward human body.

The comparison of the proposed button antenna and other wearable antennas is summarized in Table 4. It is noted that the button antenna in [44] shows the best performance in terms of efficiency and gain. In general, the proposed antenna has superior performance in terms of the number of bands, wide bandwidth with adequate radiation efficiency, gain, antenna size, SAR, polarization diversity, and radiation pattern diversity. The proposed antenna can adapt to versatile wireless applications of on-/off-body communications.

V. CONCLUSION

In this study, we present a dual-port button antenna for on-/off-body communications. The proposed antenna consists of two radiators; the crossed-bowtie dipole radiator is designed on a semi-rigid substrate, and the annular-ring radiator is designed on a felt substrate. The proposed antenna is versatile in terms of application band, communication mode, and polarization state. The proposed antenna had stable performance under bending and tilting conditions. The fabricated antenna is validated by measurement in both free space and in a phantom body environment exhibiting good agreement between simulation and measurement results. In addition, SARs for both US and European standards are evaluated showing values below the standard value. The proposed antenna is a potential candidate for multiple wireless applications.

REFERENCES

[1] T. T. Le, Y.-D. Kim, and T.-Y. Yun, "A triple-band dual-open-ring high-gain high-efficiency antenna for wearable applications," *IEEE Access*, vol. 9, pp. 118435–118442, 2021.

[2] T. Le and T.-Y. Yun, "Wearable dual-band high-gain low-SAR antenna for off-body communication," *IEEE Antennas Wireless Propag. Lett.*, vol. 20, no. 7, pp. 1175–1179, Jul. 2021.

[3] T. T. Le and T.-Y. Yun, "Miniaturization of a dual-band wearable antenna for WBAN applications," *IEEE Antennas Wireless Propag. Lett.*, vol. 19, no. 8, pp. 1452–1456, Aug. 2020.

[4] M. El Atrash, M. A. Abdalla, and H. M. Elhennawy, "A wearable dual-band low profile high gain low SAR antenna AMC-backed for WBAN applications," *IEEE Trans. Antennas Propag.*, vol. 67, no. 10, pp. 6378–6388, Oct. 2019.

[5] I. Martinez, C.-X. Mao, D. Vital, H. Shahariar, D. H. Werner, J. S. Jur, and S. Bhardwaj, "Compact, low-profile and robust textile antennas with improved bandwidth for easy garment integration," *IEEE Access*, vol. 8, pp. 77490–77500, 2020.

[6] P. Sambandam, M. Kanagasabai, R. Natarajan, M. G. N. Alsath, and S. Palaniswamy, "Miniaturized button-like WBAN antenna for off-body communication," *IEEE Trans. Antennas Propag.*, vol. 68, no. 7, pp. 5228–5235, Jul. 2020.

[7] A. Y. I. Ashyap, S. H. B. Dahlan, Z. Z. Abidin, M. H. Dahri, H. A. Majid, M. R. Kamarudin, S. K. Yee, M. H. Jamaluddin, A. Alomainy, and Q. H. Abbasi, "Robust and efficient integrated antenna with EBG-DGS enabled wide bandwidth for wearable medical device applications," *IEEE Access*, vol. 8, pp. 56346–56358, 2020.

[8] M. El Atrash, O. F. Abdalgalil, I. S. Mahmoud, M. A. Abdalla, and S. R. Zahran, "Wearable high gain low SAR antenna loaded with backed all-textile EBG for WBAN applications," *IET Microw., Antennas Propag.*, vol. 14, no. 8, pp. 791–799, Jul. 2020.

[9] A. Smida, A. Iqbal, A. J. Alazemi, M. I. Waly, R. Ghayoula, and S. Kim, "Wideband wearable antenna for biomedical telemetry applications," *IEEE Access*, vol. 8, pp. 15687–15694, 2020.

[10] S. Ahmed, D. Le, L. Sydanheimo, L. Ukkonen, and T. Bjorninen, "Wearable metasurface-enabled quasi-yagi antenna for UHF RFID reader with end-fire radiation along the forearm," *IEEE Access*, vol. 9, pp. 77229–77238, 2021.

[11] A. S. M. Sayem, R. B. V. B. Simorangkir, K. P. Esselle, R. M. Hashmi, and H. Liu, "A method to develop flexible robust optically transparent unidirectional antennas utilizing pure water, PDMS, and transparent conductive mesh," *IEEE Trans. Antennas Propag.*, vol. 68, no. 10, pp. 6943–6952, Oct. 2020.

[12] S. Yan, P. J. Soh, and G. A. E. Vandenbosch, "Wearable dual-band magneto-electric dipole antenna for WBAN/WLAN applications," *IEEE Trans. Antennas Propag.*, vol. 63, no. 9, pp. 4165–4169, Sep. 2015.

[13] G.-P. Gao, C. Yang, B. Hu, R.-F. Zhang, and S.-F. Wang, "A wearable PIFA with an all-textile metasurface for 5 GHz WBAN applications," *IEEE Antennas Wireless Propag. Lett.*, vol. 18, no. 2, pp. 288–292, Feb. 2019.

[14] Z. H. Jiang and D. H. Werner, "A compact, wideband circularly polarized co-designed filtering antenna and its application for wearable devices with low SAR," *IEEE Trans. Antennas Propag.*, vol. 63, no. 9, pp. 3808–3818, Sep. 2015.

[15] H.-R. Zu, B. Wu, Y.-H. Zhang, Y.-T. Zhao, R.-G. Song, and D.-P. He, "Circularly polarized wearable antenna with low profile and low specific absorption rate using highly conductive graphene film," *IEEE Antennas Wireless Propag. Lett.*, vol. 19, no. 12, pp. 2354–2358, Dec. 2020.

[16] X. Hu, S. Yan, and G. A. E. Vandenbosch, "Compact circularly polarized wearable button antenna with broadside pattern for U-NII worldwide band applications," *IEEE Trans. Antennas Propag.*, vol. 67, no. 2, pp. 1341–1345, Feb. 2019.

[17] A. Iqbal, A. Smida, A. J. Alazemi, M. I. Waly, N. K. Mallat, and S. Kim, "Wideband circularly polarized MIMO antenna for high data wearable biotelemetric devices," *IEEE Access*, vol. 8, pp. 17935–17944, 2020.

[18] U. Ullah, I. B. Mabrouk, and S. Koziel, "A compact circularly polarized antenna with directional pattern for wearable off-body communications," *IEEE Antennas Wireless Propag. Lett.*, vol. 18, no. 12, pp. 2523–2527, Dec. 2019.

[19] K. W. Lui, O. H. Murphy, and C. Toumazou, "A wearable wideband circularly polarized textile antenna for effective power transmission on a wirelessly-powered sensor platform," *IEEE Trans. Antennas Propag.*, vol. 61, no. 7, pp. 3873–3876, Jul. 2013.

[20] J. Zhang, J. Meng, W. Li, S. Yan, and G. A. E. Vandenbosch, "A wearable button antenna sensor for dual-mode wireless information and power transfer," *Sensor*, vol. 21, no. 17, pp. 1–15, Jun. 2021.

[21] K. N. Paracha, S. K. A. Rahim, P. J. Soh, M. R. Kamarudin, K.-G. Tan, Y. C. Lo, and M. T. Islam, "A low profile, dual-band, dual polarized antenna for indoor/outdoor wearable application," *IEEE Access*, vol. 7, pp. 33277–33288, 2019.

[22] B. Sanz-Izquierdo, J. A. Miller, J. C. Batchelor, and M. I. Sobhy, "Dual-band wearable metallic button antennas and transmission in body area networks," *IET Microw., Antennas Propag.*, vol. 4, no. 2, pp. 182–190, Feb. 2010.

[23] X. Hu, S. Yan, J. Zhang, V. Volski, and G. A. E. Vandenbosch, "Omnidirectional circularly polarized button antenna for 5 GHz WBAN applications," *IEEE Trans. Antennas Propag.*, vol. 69, no. 8, pp. 5054–5059, Aug. 2021.

[24] A. Paraskevopoulos, D. de Sousa Fonseca, R. D. Seager, W. G. Whittow, J. C. Vardaxoglou, and A. A. Alexandridis, "Higher-mode textile patch antenna with embroidered vias for on-body communication," *IET Microw., Antennas Propag.*, vol. 10, no. 7, pp. 802–807, May 2016.

[25] B. Mohamadzade, R. B. V. B. Simorangkir, R. M. Hashmi, Y. Chao-Oger, M. Zhadobov, and R. Sauleau, "A conformal band-notched ultrawideband antenna with monopole-like radiation characteristics," *IEEE Antennas Wireless Propag. Lett.*, vol. 19, no. 1, pp. 203–207, Jan. 2020.

[26] K. Agarwal, Y.-X. Guo, and B. Salam, "Wearable AMC backed near-endfire antenna for on-body communications on latex substrate," *IEEE Trans. Compon., Packag., Manuf. Technol.*, vol. 6, no. 3, pp. 346–358, Mar. 2016.

[27] A. Arif, M. Zubair, M. Ali, M. U. Khan, and M. Q. Mehmood, "A compact, low-profile fractal antenna for wearable on-body WBAN applications," *IEEE Antennas Wireless Propag. Lett.*, vol. 18, no. 5, pp. 981–985, May 2019.

[28] A. Alemaryeen and S. Noghanian, "On-body low-profile textile antenna with artificial magnetic conductor," *IEEE Trans. Antennas Propag.*, vol. 67, no. 6, pp. 3649–3656, Jun. 2019.

[29] H. Xiaomu, S. Yan, and G. A. E. Vandenbosch, "Wearable button antenna for dual-band WLAN applications with combined on and off-body radiation patterns," *IEEE Trans. Antennas Propag.*, vol. 65, no. 3, pp. 1384–1387, Mar. 2017.

[30] L. Zhou, S. Fang, and X. Jia, "Dual-band and dual-polarised circular patch textile antenna for on-/off-body WBAN applications," *IET Microw., Antennas Propag.*, vol. 14, no. 7, pp. 643–648, Jun. 2020.

[31] R. B. V. B. Simorangkir, Y. Yang, L. Matekovits, and K. P. Esselle, "Dual-band dual-mode textile antenna on PDMS substrate for body-centric communications," *IEEE Antennas Wireless Propag. Lett.*, vol. 16, pp. 677–680, 2017.

[32] X. Yin, S. J. Chen, and C. Fumeaux, "Wearable dual-band dual-polarization button antenna for WBAN applications," *IEEE Antennas Wireless Propag. Lett.*, vol. 19, no. 12, pp. 2240–2244, Dec. 2020.

[33] X. Y. Zhang, H. Wong, T. Mo, and Y. F. Cao, "Dual-band dual-mode button antenna for on-body and off-body communication," *IEEE Trans. Biomed. Circuits Syst.*, vol. 11, no. 4, pp. 933–941, Aug. 2017.

[34] S. Yan and G. A. E. Vandenbosch, "Radiation pattern-reconfigurable wearable antenna based on metamaterial structure," *IEEE Antennas Wireless Propag. Lett.*, vol. 15, pp. 1715–1718, 2016.

[35] X. Tong, C. Liu, X. Liu, H. Guo, and X. Yang, "Switchable ON-/OFF-body antenna for 2.45 GHz WBAN applications," *IEEE Trans. Antennas Propag.*, vol. 66, no. 2, pp. 967–971, Feb. 2018.

[36] H. Wong, W. Lin, L. Huitema, and E. Arnaud, "Multi-polarization reconfigurable antenna for wireless biomedical system," *IEEE Trans. Biomed. Circuits Syst.*, vol. 11, no. 3, pp. 652–660, Jun. 2017.

[37] H. Sun, Y. Hu, R. Ren, L. Zhao, and F. Li, "Design of pattern-reconfigurable wearable antennas for body-centric communications," *IEEE Antennas Wireless Propag. Lett.*, vol. 19, no. 8, pp. 1385–1388, Aug. 2020.

[38] R. Masood, C. Person, and R. Sauleau, "A dual-mode, dual-port pattern diversity antenna for 2.45-GHz WBAN," *IEEE Antennas Wireless Propag. Lett.*, vol. 16, pp. 1064–1067, 2017.

[39] C. Mendes and C. Peixeiro, "A dual-mode single-band wearable microstrip antenna for body area networks," *IEEE Antennas Wireless Propag. Lett.*, vol. 16, pp. 3055–3058, 2017.

[40] C. Mendes and C. Peixeiro, "On-body transmission performance of a novel dual-mode wearable microstrip antenna," *IEEE Trans. Antennas Propag.*, vol. 66, no. 9, pp. 4872–4877, Sep. 2018.

[41] K. Zhang, Z. H. Jiang, W. Hong, and D. H. Werner, "A low-profile and wideband triple-mode antenna for wireless body area network concurrent on-/off-Body communications," *IEEE Trans. Antennas Propag.*, vol. 68, no. 3, pp. 1982–1994, Mar. 2020.

[42] B. Sanz-Izquierdo, J. C. Batchelor, and M. I. Sobhy, "Button antenna on textiles for wireless local area network on body applications," *IET Microw., Antennas Propag.*, vol. 4, no. 11, pp. 1980–1987, 2010.

[43] S. Yan and G. A. E. Vandenbosch, "Design of wideband button antenna based on characteristic mode theory," *IEEE Trans. Biomed. Circuits Syst.*, vol. 12, no. 6, pp. 1383–1391, Dec. 2018.

[44] J. Zhang, S. Yan, X. Hu, and G. A. E. Vandenbosch, "Dual-band dual-polarized wearable button array with miniaturized radiator," *IEEE Trans. Biomed. Circuits Syst.*, vol. 13, no. 6, pp. 1583–1592, Dec. 2019.

[45] Y. S. Yu and F. J. Rosenbaum, "Mode chart for microstrip ring resonators," *IEEE Trans. Microw. Theory Techn.*, vol. MTT-21, no. 7, pp. 487–489, Jul. 1973.

TU TUAN LE received the B.S. degree in electronics and telecommunications from the Hanoi University of Science and Technology, Hanoi, Vietnam, in 2013, and the Ph.D. degree from the Department of Electronics and Electrical Engineering, Dongguk University, Seoul, South Korea. He is currently with Hanyang University, Seoul, as a Research Assistant Professor. His current research interests include RF energy harvesting, wearable antenna, circularly polarized antennas, reconfigurable antennas, and multiband/broadband planar antennas for various wireless applications.

YONG-DEOK KIM received the B.S. degree in information and communication engineering from Hoseo University, South Korea, in 2020. He is currently pursuing the Ph.D. degree with the Department of Electronics engineering, Hanyang University, Seoul, South Korea. His current research interests include circularly polarized antennas, wearable antennas, multiband antennas, and on-chip antennas for various wireless applications.

TAE-YEOUL YUN (Member, IEEE) received the Ph.D. degree from the Department of Electrical Engineering, Texas A&M University, College Station, TX, USA, in 2001. From 1989 to 1996, he worked with the Optical Telecommunication System Group, ETRI, Daejon, South Korea, where he developed 2.5- and 10-Gb/s systems. From 2001 to 2003, he was a MMIC Designer at Triquint Semiconductor, Dallas, TX, USA. Since 2003, he has been a Professor at Hanyang University, Seoul, South Korea. His research interests include RFICs, antennas, and wireless/optical high-speed communication systems.